

# Hybrid stress analysis of a near-surface circular hole in finite structures

Abdullah Alshaya<sup>1</sup>  and Shiang-Jiun Lin<sup>2</sup>

*Proc IMechE Part C:  
J Mechanical Engineering Science*  
2020, Vol. 234(7) 1366–1381  
© IMechE 2019  
Article reuse guidelines:  
[sagepub.com/journals-permissions](http://sagepub.com/journals-permissions)  
DOI: 10.1177/0954406219892995  
[journals.sagepub.com/home/pic](http://journals.sagepub.com/home/pic)



## Abstract

The ability to stress-analyze complicated structures from recorded load-induced temperatures is demonstrated. The considered structures have a near-surface hole and subjected to a concentrated load. The complexity of the structure is simplified by conformal mapping, the traction-free condition on the boundary of the hole is analytically satisfied by analytic continuation, and the equilibrium and compatibility conditions are satisfied by means of Airy stress function in complex-variable formulation. For isotropic member that is cyclically loaded within its elastic range, the produced in-phase temperature variations are linearly proportional to the local changes in the normal stresses. Even though no recorded thermal data were used at or near to the edges, the present hybrid method simultaneously separates the load-induced temperatures into the individual stress components, determines reliably the boundary stress and hence the stress concentration, and smooths the measured input data. Unlike prior capabilities of using geometrical symmetry to simply the stress function representation, the present analysis retains all the terms in the stress functions. Therefore, the considered hybrid stress analysis approach of such complex structures extends significantly the applicability of thermoelastic stress analysis compared to prior capabilities and is considered to be the most complicated formulation of the hybrid complex-variable method to date. To support the reliability of the present hybrid method, the results were compared with finite element predictions and previous results based on Mitchell solution.

## Keywords

Thermoelastic stress analysis, hybrid method, thermal analysis, airy stress function, complex-variable method

Date received: 3 June 2019; accepted: 6 November 2019

## Introduction

The structural integrity is controlled by the high stresses and their gradients at the geometrical discontinuity which often lead to component failure. The complexity of the stress distribution near a discontinuity in finite structures and the unreliability of the boundary conditions can preclude the use of purely theoretical and/or numerical techniques. Traditional experimental stress analysis techniques, e.g., moiré, strain gages, holography, photoelastic stress analysis (PSA), thermoelastic stress analysis (TSA), and digital image correlation (DIC), can be used to provide stress information in such cases. However, displacement-based experimental techniques require a physical differentiation of the measured data, something which can be unreliable, whereas PSA and TSA both require a separation process of the measured data (isochromatic fringe patterns or isopachic thermal patterns) into the three individual stress components. The load-induced temperatures (sometimes called thermal measurements or thermoelastic signals) from TSA can be combined with other experiment like PSA or numerical techniques like finite-element,

finite-difference, or boundary-collocation methods to separate the thermoelastic signals into the individual stresses.<sup>1–3</sup> However, utilizing only a single experimental technique (TSA for the case here) to acquire all the necessary stress data is desirable and competent.

TSA is an experimental stress analysis technique that is noncontacting, nondestructive, and full-field (unlike strain gages). Unlike traditional photoelasticity which requires test modeling, the TSA can be used to stress-analyze structures in their operating environment. For an isotropic member that is cyclically loaded within its elastic range to ensure reversible

<sup>1</sup>Department of Mechanical Engineering, Kuwait University, Safat, Kuwait

<sup>2</sup>Department of Mechanical Engineering, National Kaohsiung University of Science and Technology, Kaohsiung

### Corresponding author:

Abdullah Alshaya, Department of Mechanical Engineering, College of Engineering and Petroleum, Kuwait University, P.O. Box 5969, Safat 13060, Kuwait.

Email: [abdullah.alshaya@ku.edu.kw](mailto:abdullah.alshaya@ku.edu.kw)

and adiabatic conditions, the produced in-phase temperature variations are linearly proportional to the local changes in the normal stresses.<sup>4,5</sup> The load-induced temperature changes can be recorded from a sensitive infrared detector. The availability of commercial software and hardware renders TSA efficient with a sensitivity equivalent to that of strain gages and the ability to rapidly record and process large amounts of measured information. Unlike displacement-based experiment, TSA does not require to physically differentiate the measured data. In contrast to DIC, TSA does not require a speckle pattern on the surface of the tested structure. Virtually, no component preparation is needed only perhaps a flat black paint to provide an enhanced and uniform emissivity of the tested structure's surface. However, TSA does require a cyclic loading of the structure under study to sufficiently minimize the heat transfer in the specimen in order to obtain adiabatic and reversible conditions.

Wang et al.<sup>6</sup> show the similarity between the recorded and reconstructed isochromatic fringe patterns around a near-surface circular hole in a semi-infinite plate under a concentrated load. The loaded plates in Figure 1(a) and (b) were previously stress-analyzed by hybridizing the thermal information with the Mitchell solution.<sup>7-9</sup> The Mitchell solution, which is the general solution of biharmonic equation in polar coordinates with assumption of periodic solution, consists of an infinite number of coefficients and its form depends on the geometry, loading, and boundary conditions, whether the component is boundedness at origin or infinity, and single-valued stresses and displacements. The coefficients can also be reduced by imposing the traction-free condition analytically along the boundary of the hole.<sup>10</sup> The thermal signals in conjunction with the Mitchell solution were hybridized to determine the full-field stress for different geometrical discontinuities and loading conditions.<sup>11-14</sup> The individual stresses in a tensile loaded plate containing a single-sided deep U-notch were experimentally determined from recorded

load-induced and the full form of the Mitchell solution.<sup>15</sup> Recently, a finite, complicated-shaped plate containing an asymmetrical, irregularly shaped hole was thermally stress-analyzed while imposing the traction-free conditions on the internal and external boundaries.<sup>16</sup> Singh and Bhandakkar<sup>17</sup> proposed a simple approach based on Mitchell solution to solve problems with mixed boundary conditions. Using the complex-variable method (CVM), the stress distribution around several cutouts in finite structures was determined using stress function and mapping techniques.<sup>18,19</sup>

Unlike the hybrid method based on Mitchell solution, which is limited to isotropic response, the CVM, based on analytic continuation and mapping techniques, were extensively used to evaluate reliable hybrid stresses in loaded isotropic and orthotropic components on the boundary of different geometrical discontinuities (side notch, circular hole, elliptical hole) and stress intensity factors in cracks from different experimental techniques: thermoelastic data,<sup>20-24</sup> photoelastic data,<sup>25</sup> strains,<sup>26</sup> and displacements.<sup>27,28</sup> The hybrid method based on complex-variable formulation is suitable for finite (can be difficult theoretically) and infinite geometries. Advantages over other such hybrid analyses include the fact that this hybrid method based on complex-variable formulation satisfies the equilibrium, compatibility, and local boundary conditions; requires few measured input data which can be arbitrarily located; requires few terms in the stress function representation; does not necessitate knowing the entire boundary, distant loading conditions, or material elastic constants; applies for isotropic and anisotropic responses; smooths the original measured input data; enhances the edge information; and determines the individual full-field stresses, strains, and displacements throughout, including on the edge of the hole, even though no information were used there. The complexity of the geometry was simplified by involving conformal mappings, and the traction-free conditions around the

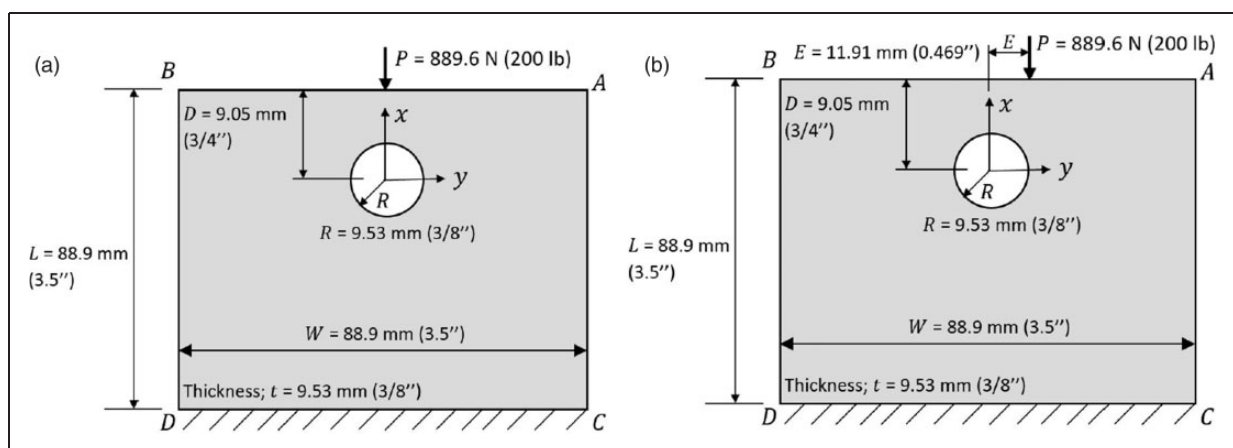


**Figure 1.** Plate containing a near-surface circular hole subjected to (a) a central and (b) an offset concentrated load.

near-edge hole were analytically satisfied using analytic continuation.

Unlike the previous approaches<sup>7–9</sup> where their analyses utilized complicated and restrictive stress functions because of the asymmetry about the  $x$ - or  $y$ -axes, the present analysis uses only one form of the stress function to solve both the central- and offset-loaded plates (Figure 1(a) and (b)). The advantageous of using this approach is considered to be more general and substantially involve simpler formulation than the previous approaches based on Mitchell solution. Although the effect of the external applied load is implicitly included in the measured data, previous approaches<sup>7,8</sup> explicitly accounted for the effect of the load and consequently formulated a complicated stress function. In contrast with the prior applications of the CVM while utilizing geometrical and loading symmetry to retain only the odd and real coefficients of the stress function, the present method considers asymmetrical cases, which necessitate retaining all the terms in the stress function. The unsymmetrical case of the plate in Figure 1(b) where the applied load is offset horizontally from the central hole significantly extends thermoelastic applicability of the hybrid-CVM beyond prior capabilities of using geometrical symmetry. Unlike the approach of Hawong et al.<sup>25</sup> which utilized photoelastic isochromatic method that requires non-linear least squares, the present method that uses the measured isopachics requires only linear least-squares.

A major contribution of this paper is to demonstrate the ability of the CVM to experimentally stress-analyze complex structures with lack of symmetry and consequently wide applicability of this hybrid approach. The TSA-hybrid method described here does not necessitate any supplemental experimental information (such as measured displacements, strain gages, isoclinics, or isochromatics) is also desirable and competent. The current study is the most complicated stress analysis formulation to date. The authors are unaware of any previous use of thermoelastic signals (temperature measurements) in conjunction with CVM to evaluate the individual stresses in a complex structure such as the finite plate with a near-surface hole.

The plan of the paper is organized as follows: first, the details of the TSA are explained; the experimental details including the plate dimensions, preparation, loading conditions, data calibration, data acquisitions, and data processing are then introduced; the formulation of the CVM and the determination of the unknown complex coefficients are then presented; the obtained results and the comparison with other approaches are illustrated; and finally, the discussion and conclusion of the paper are drawn.

## Thermoelastic stress analysis

TSA is an experimental technique that is based on measuring the small temperatures changes (in order

of mK) for determining the related full-field stresses in loaded members.<sup>1–5</sup> For an isotropic specimen that is cyclically loaded within its elastic range to sufficiently minimize the heat transfer in the specimen in order to obtain adiabatic and reversible conditions, the thermoelastic system signals,  $S^*$ , are linearly related to the change in sum of the normal stresses (isopachic stress) on the specimen surface<sup>29</sup>

$$S^* = K\Delta(\sigma_{xx} + \sigma_{yy}) = K\Delta(\sigma_p + \sigma_q) = K\Delta(\sigma_{rr} + \sigma_{\theta\theta}) \quad (1)$$

where  $K$  is an experimentally-determined thermomechanical calibration coefficient, and  $\sigma_p$ ,  $\sigma_q$ ,  $\sigma_{rr}$ ,  $\sigma_{\theta\theta}$ ,  $\sigma_{xx}$ , and  $\sigma_{yy}$ , are the stresses in the principal, polar, and Cartesian rectangular coordinates, respectively. The calibration coefficient  $K$  depends on the radiometric properties of the detector, physical material properties, surface conditions, and TSA system variables.<sup>30</sup> Therefore, the calibration coefficient can be determined either by using detector/material properties, from a calculated stress with known applied load (this approach was used here), or from an independent measure of stress perhaps using strain gages.

Since TSA signals give the thermal information that is related to the sum of the normal stresses, it is required to separate the stresses. Additionally, TSA measured information can be noisy and involve some scatter and the recorded TSA signals at, and adjacent to, an edge are typically unreliable. The reason behind the unreliability of the edge information is because of the motion of the structure and its edges due to the cyclic loading. Even if one uses a high magnification and has a high spatial resolution, the detector sees the pixel at the edges as a spot which is partly on the stressed structure and partly on the stress-free background. The cyclic loading of the structure, and hence its edges, will also provide different data to the detector from different spatial positions. The high-stress gradients at such location will typically violate the adiabatic condition and exhibit the accurately of the edge stresses thermoelastically, and hence accurate stress concentrations.

The present hybrid technique overcomes these challenges by avoiding the use of recorded data on and near the edges and only processing the interior measured data with a CVM. The full-field stresses were determined including on the boundary without the full knowledge of the applied load, the distant geometry, or material elastic properties. Without the need of satisfying the external boundary conditions beyond the traction-free conditions at the hole, the present technique accurately predicts the boundary stresses.

## Experimental details

For sake of completeness, a brief description of the experimental set-up is included here where the

thorough details are given in Lin.<sup>31</sup> The TSA equipment and system specification are listed in Table 1. The following sections discuss the preparation of plate, the condition of the applied loading, the calibration of the TSA, and the TSA data acquisition and processing.

### Plate geometry and loading conditions

The developed hybrid-TSA approach based on CVM is utilized to stress-analyze a square Aluminum (6061 T6511) plate containing a near-surface hole as shown in Figure 1(a) and (b). The plate with a height of  $L = 88.9 \text{ mm}$  (3.5"), a width of  $W = 88.9 \text{ mm}$  (3.5") and a thickness of  $t = 9.53 \text{ mm}$  (3/8") has a near-surface hole of radius  $R = 9.53 \text{ mm}$  (3/8") located at a distance  $D = 9.05 \text{ mm}$  (3/4") below the surface. The coordinate origin is located at the center of the hole, where the  $x$ - and  $y$ -axes are along the vertical and horizontal directions, respectively. In order to maintain minimum heat transfer in the specimen to achieve reversible and adiabatic conditions, the plate was loaded physically through a piece of round drill rod in a 90 kN (20,000 lb) capacity MTS hydraulic testing machine with a cyclically varying sinusoidal load with a mean value of 889.6 N (200 lb), maximum value of 222.4 N (50 lb), and minimum value of 1112 N (250 lb) at 20 Hz. The plate in Figure 1(a) was supported along the bottom edge, CD, and subjected to the concentrated load directly above the near-surface hole, i.e.,  $y = 0$ . Therefore, the response for this case can be considered symmetric along the vertical  $x$ -axis. The plate was then subjected to an offset surface-load away from the near-surface hole by a horizontal distance  $E = 11.91 \text{ mm}$  ( $=0.469"$ ), i.e.,  $y = E$ , as shown in Figure 1(b). To ensure maintaining adiabatic and reversible conditions, the phase information was also monitored.

**Table 1.** Technical information about the TSA equipment and system.

Parameter	Setting
TSA model	Delta Therm model DT1410 infrared camera
Supplier	Stress Photonics, Madison, WI
Data acquisition system	Delta Vision Software
Infrared camera	
Specification	Indium antimonide (InSb) focal-plane array
Sensor	256 horizontal by 256 vertical pixels
Range	3–5 $\mu\text{m}$ with a peak response at a wavelength of 5.3 $\mu\text{m}$
Speed	1000 frames/s
Resolution	0.001 $^{\circ}\text{C}$

### Plate preparation

Prior testing the plate in Figure 1(a) and (b), the surface of the plate was initially polished by a grit sand paper, and then sprayed with Krylon Ultra-Flat black paint to provide enhanced and uniform emissivity. When sanding the surface of the plate, precaution was taken to not round-off the edge of the hole which could further erode the quality of the thermal information.

### TSA recording and data processing

The load-induced temperature variations were recorded using a liquid-nitrogen cooled TSA Delta Therm model DT1410 infrared camera (Stress Photonics, Madison, WI; Table 1). The camera detectors were cooled to 77 K with liquid nitrogen. From the total provided 65,536 discrete TSA signals, there are approximately 14,500–15,000 available values in the loaded structures. The recorded thermoelastic signals,  $S^*$ , from Delta Vision Software throughout the plates in Figure 1(a) and (b) induced by cyclically varying loading are shown in Figures 2 and 3, respectively. TSA images were captured and averaged over a duration of 2 min, and then exported and converted each pixel into a data point, i.e., 256 by 256 matrix. The size of a pixel is 0.73 mm (0.029 in.).

Since the plate behavior of Figure 1(a) is symmetrical about the vertical  $x$ -axis, the recorded TSA signals in the right and left regions of Figure 2 were averaged. The unreliability TSA data on and near the external and hole edges were discarded and only the 300 and 849 TSA signals shown in Figure 2 for the plate in Figure 1(a) and in Figure 3 for the plate in Figure 1(b), respectively, were used for the current stress analysis. These regions will be denoted as  $R^*$  for the rest of the paper. Although the source locations of TSA data in region  $R^*$  are largely arbitrary, the thermal data captures the high stress region originated by the concentrated load,  $P$ , and the hole. The hybrid method based on CVM provides reliable stress from few arbitrary located measured data.<sup>28</sup> Data of Figures 2 and 3 originate at least 4 pixels (approximately 3 mm) away from the boundary of the hole and the top edge of Figure 1(a) and (b), respectively.

### TSA calibration

The thermomechanical calibration coefficient,  $K$ , of equation (1) can only be obtained from the tested plate of Figure 1(a) and (b) if there is a region of known uniform stress. Since there is no such region, the calibration coefficient was experimentally determined from a different supplementary uniaxial tensile Aluminum coupon loaded in the vertical direction. The coupon was initially polished by a grit sand paper, sprayed with the same paint, i.e., Krylon Ultra-Flat black, subjected to sinusoidal loading at 20 Hz, and tested on the same day of testing the



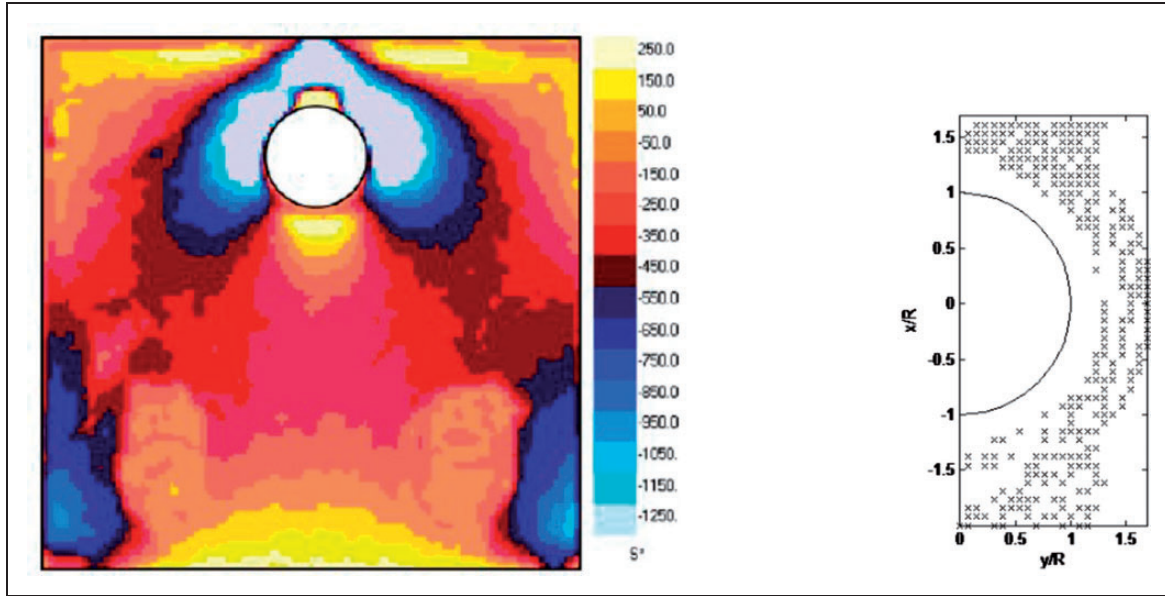


**Figure 2.** Thermoelastic data source locations ( $m = 300$  data points) for the plate in Figure 1(a) (reprinted from Lin et al.,<sup>7</sup> with kind permission from Springer Science and Business Media).

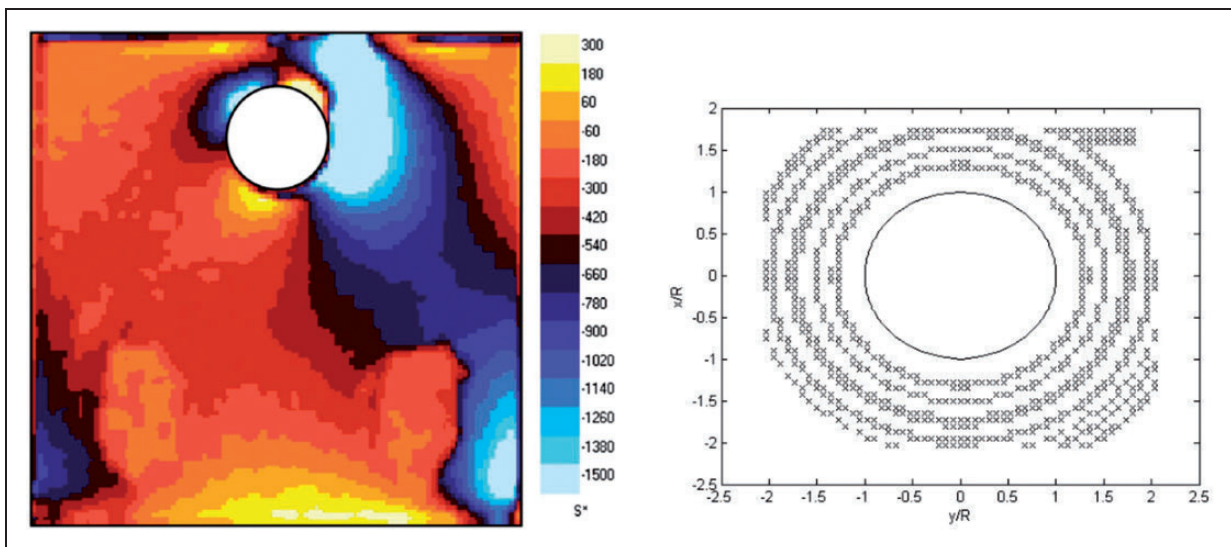


**Figure 3.** Thermoelastic data source locations ( $m = 849$  data points) for the plate in Figure 1(b) (reprinted from Lin et al.,<sup>8</sup> with kind permission from Elsevier).

plate in Figure 1(a) and (b). The TSA signals were monitored and recorded using the same TSA infrared system (Stress Photonics). The value of thermomechanical coefficient,  $K$ , was determined from equation (1) to be  $K = 319 \text{ U/MPa}$  ( $2.21 \text{ U/psi}$ ). In uncalibrated TSA signal units, the unit  $U$  is used to signify the raw data.

The isopachic stress, i.e.,  $\sigma_{xx} + \sigma_{yy} = \sigma_{rr} + \sigma_{\theta\theta}$ , can be determined by dividing the recorded TSA signals of Figures 2 and 3 by the calibration coefficient,  $K$ . The objective of this paper is to separate the isopachic stress into the three individual stress components and provide reliable stresses adjacent to the near-surface hole. An analytical expression of the isopachic stress based on CVM and Laurent series expansion was

equated to the TSA recorded isopachic stress and from which the unknown coefficients of the series expansion can be evaluated in a least-squares sense. Since the recorded  $S^*$  values may include some noise, it was intended to collect tensile TSA signals larger than the number of retained unknown coefficients. Recognizing the most important stresses occur on or near the boundary of the near-surface hole, only its adjacent region, rather than the entire plate, was considered.

### Relevant equations

The method behind determining the state of stress at and near the surface-hole lies in coupling the

measured thermoelastic data of Figures 2 and 3 with a series representation of stress function in terms of complex-variable formulation, and hence the term *hybrid*.

### Formulation of CVM

The plane stresses in the Cartesian coordinates  $(x, y)$  of the physical  $z(=x+iy)$  plane in orthotropic media with the absence of body forces can be written as<sup>32,33</sup>

$$\sigma_{xx} = 2\Re[\mu_1^2\Phi'(z_1) + \mu_2^2\Psi'(z_2)] \quad (2a)$$

$$\sigma_{yy} = 2\Re[\Phi'(z_1) + \Psi'(z_2)] \quad (b)$$

$$\sigma_{xy} = -2\Re[\mu_1\Phi'(z_1) + \mu_2\Psi'(z_2)] \quad (c)$$

where primes denote differentiation with respect to the argument,  $\Phi(z_1)$  and  $\Psi(z_2)$  are the two arbitrary analytic stress functions,  $z_j = x + \mu_j y$  for  $j=1, 2$  and  $\Re$  denotes the “real part” of a complex number. The stresses of equations (2) satisfy equilibrium and the associated strains satisfy compatibility. The complex material properties  $\mu_1$  and  $\mu_2$  are two distinct roots of the following characteristic equation associated with the compatibility equation

$$\mu^4 + \left(\frac{E_1}{G_{12}} - 2\nu_{12}\right)\mu^2 + \frac{E_1}{E_2} = 0 \quad (3)$$

where  $E_1$  and  $E_2$  are the elastic moduli parallel and perpendicular to the strongest/stiffest material direction,  $G_{12}$  is the shear modulus, and  $\nu_{12}$  is Poisson's ratio. The roots of this characteristic equation are complex with  $\mu_1 = \alpha + i\beta$ ,  $\mu_2 = \gamma + i\delta$ ,  $\mu_3 = \bar{\mu}_1$ , and  $\mu_4 = \bar{\mu}_2$ . Quantities  $\alpha$ ,  $\beta$ ,  $\gamma$ , and  $\delta$  are real numbers and both  $\beta$  and  $\delta$  are positive. It is convenient to initially formulate the equations for orthotropy as they can subsequently be reduced for isotropic response. In case of isotropic material,  $E_1 = E_2 = E$ ,  $\nu_{12} = \nu$  and  $G_{12} = G = E/2(1+\nu)$ , the complex properties are  $\mu_{1,2} = \pm i$ , and hence,  $z_1 = z_2 = z = x + iy$ .

Plane problems of elasticity classically involve determining the stress functions,  $\Phi(z_1)$  and  $\Psi(z_2)$ , throughout a component subjected to the boundary conditions around its entire edge. The concept of conformal mapping and analytic continuation techniques is to relate the two stress functions to each other throughout a region  $R_z$  containing a traction-free boundary  $\Gamma$ .<sup>34</sup> Once the two functions are related, the stresses of equations (2) can be therefore expressed by a single stress function,  $\Phi(z_1)$  or  $\Psi(z_2)$ . Expressing the individual stresses in terms of a single stress function renders the stress function to be represented by a truncated power-series expansion. Rather than determining the coefficients of the series expansion by satisfying the entire boundary conditions, the coefficients can be determined from experimental

data in a least-squares sense. Other boundary and symmetrical conditions can also be satisfied discretely if the region of interest is large enough. Once the coefficients are evaluated, hence the stress functions  $\Phi(z_1)$  and  $\Psi(z_2)$ , the stresses can be determined throughout a component from equations (2).

The concept of the hybrid CVM is based on collecting measured data in a region  $R^*$  adjacent to an traction-free edge, mapping such a complicated shape into a more simpler shape such that traction-free edge is mapped into the unit circle whereby the traction-free conditions are satisfied continuously, relating the two complex stress functions to each other by means of analytic continuation, plus satisfying other loading or boundary conditions discretely on the boundary of the component beyond the traction-free conditions.

**Conformal mapping.** The complex geometry of the plate in Figure 1(a) and (b) was simplified by introducing a conformal mapping. This concept is based on mapping the region  $R_z$  of a complicated physical  $z = x + iy$  shape of a loaded component into a region  $R_\zeta$  of a simpler shape in the  $\zeta = \xi + i\eta$  plane, the latter being a unit circle (Figure 4).<sup>34,35</sup> This simplified geometry in the  $\zeta$ -mapped domain is chosen to aid in solving the equations, and once the results are obtained it will be mapped back to the original  $z$ -physical geometry as a valid solution.

Assume that a mapping function of the form  $z = \omega(\zeta)$  exists and which maps  $R_\zeta$  of the exterior of a unit circle in  $\zeta = \xi + i\eta$  plane into  $R_z$  of a finite plate having a hole in physical  $z = x + iy$  plane of a loaded component (Figure 4). For orthotropy, auxiliary planes and their induced mapping functions are defined in terms of  $\zeta_j = \xi + \mu_j\eta$ ; therefore,  $z_j = \omega_j(\zeta_j)$ , for  $j=1, 2$ . The induced conformal mapping functions are, therefore, one-to-one and invertible. The stress functions  $\Phi(z_1)$  and  $\Psi(z_2)$  can be expressed as the following analytic functions of  $\zeta_1$  and  $\zeta_2$ , respectively,

$$\begin{aligned} \Phi(z_1) &= \Phi[\omega_1(\zeta_1)] \equiv \Phi(\zeta_1) \text{ and } \Psi(z_2) \\ &= \Psi[\omega_2(\zeta_2)] \equiv \Psi(\zeta_2) \end{aligned} \quad (4)$$

The derivatives of these stress functions with respect to their argument are

$$\Phi'(z_1) = \Phi'(\zeta_1) \frac{d\zeta_1}{dz_1} = \frac{\Phi'(\zeta_1)}{\omega'_1(\zeta_1)} \text{ and } \Psi'(z_2) = \frac{\Psi'(\zeta_2)}{\omega'_2(\zeta_2)} \quad (5)$$

The analyticity of the mapping functions certifies that equilibrium and compatibility equations are satisfied throughout region  $R_z$  of the physical plane.

**Mapping formulation.** The concept here is to apply this analysis to any region  $R_z$  adjacent to a traction-free boundary  $\Gamma$  of a component provided an appropriate

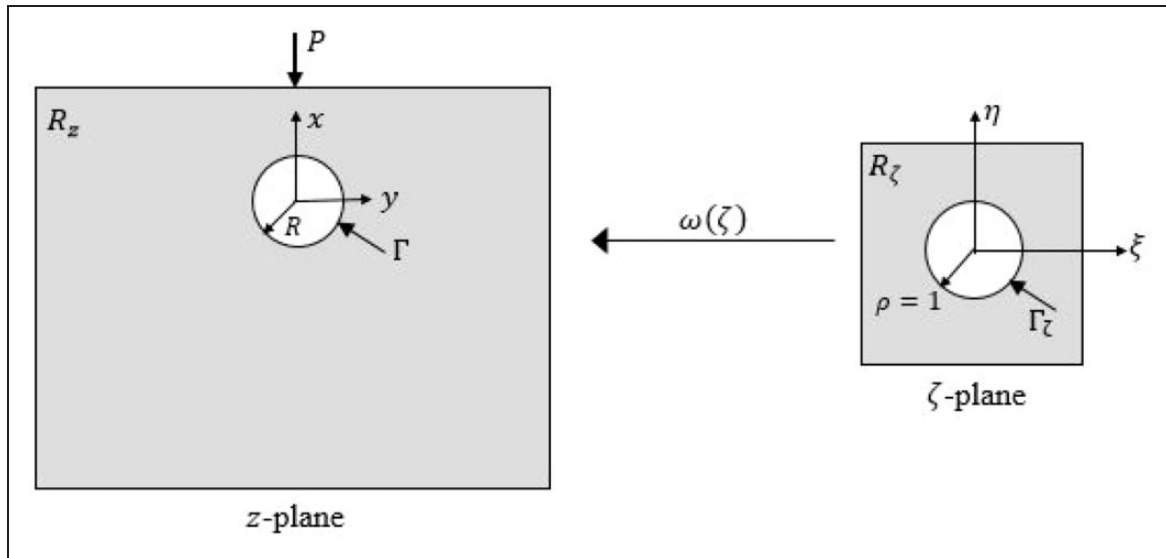


**Figure 4.** The mapping of the current structure in the physical  $z$ -plane into the exterior region of a unit circle in  $\zeta$ -plane.

mapping function is available to map the region  $R_\zeta$  into region  $R_z$ .

### Circular cutouts

For a region  $R_z$  adjacent to a circular cutout of radius  $R$ , the following function

$$z_j = \omega_j(\zeta_j) = \frac{R}{2} \left[ (1 - i\mu_j)\zeta_j + \frac{1 + i\mu_j}{\zeta_j} \right] + z_j^c, \quad (6)$$

$j = 1, 2$

maps the region of the exterior of a unit circle,  $R_\zeta$ , of the  $\zeta$ -plane into the region  $R_z$  of the  $z$ -physical plane, where  $z_j^c$  is the center location of the circular cutout  $z_j^c = x_c + \mu_j y_c$  (Figure 4). For convenience, the coordinate system can be chosen such that the origin is at the center of the circle, i.e.,  $z_c = 0$ . The inverse of the induced mapping functions is

$$\zeta_j = \omega_j^{-1}(z_j) = \frac{(z_j - z_j^c) \pm \sqrt{(z_j - z_j^c)^2 - R^2(1 + \mu_j^2)}}{R(1 - i\mu_j)}, \quad (7)$$

$j = 1, 2$

The branch of the square root in equation (7) is chosen such that  $|\zeta_j| \geq 1$  for  $j = 1, 2$ .

**Traction-free boundary.** Using the concept of analytic continuation, the individual stress functions for a region  $R_\zeta$  adjacent to a traction-free boundary of the unit circle  $\Gamma_\zeta$  of an orthotropic material are related by<sup>34,35</sup>

$$\Psi(\zeta_2) = \overline{B\Phi(1/\bar{\zeta}_2)} + C\Phi(\zeta_2) \quad (8)$$

where constants  $B$  and  $C$  are

$$B = \frac{\bar{\mu}_2 - \bar{\mu}_1}{\mu_2 - \bar{\mu}_2}, \quad C = \frac{\bar{\mu}_2 - \mu_1}{\mu_2 - \bar{\mu}_2} \quad (9)$$

Equation (8) enables the elastic state of the structure to be expressed in terms of a single stress function,  $\Phi(\zeta_1)$ , the latter which can be represented by a Laurent series expansion. Equation (8) assumes ability to map the physical boundary of interest into the unit circle in the mapped plane. Literature<sup>36</sup> contains a simple, clear derivation of equation (8).

**Mapping collocation.** The single stress function  $\Phi(\zeta_1)$  can be expressed as the following finite Laurent series

$$\Phi(\zeta_1) = \sum_{\substack{k=-N \\ k \neq 0}}^N A_k \zeta_1^k \quad (10)$$

where  $A_k = a_k + ib_k$  are the unknown complex coefficients ( $a_k$  and  $b_k$  are both real numbers). The  $k = 0$  term in the Laurent expansion contributes to rigid-body motion and can be omitted. Substituting equation (10) into (8) gives

$$\Psi(\zeta_2) = \sum_{\substack{k=-N \\ k \neq 0}}^N (B\bar{A}_k \zeta_2^{-k} + CA_k \zeta_2^k) \quad (11)$$

where  $\bar{A}_k$  is a complex conjugate of  $A_k$ . At least for a finite, simply connected region  $R_\zeta$ ,  $\Phi(\zeta_1)$  is a single-valued analytic function. Upon combining equations (2) with equations (10) and (11), the individual stresses can be expressed as

$$\sigma_{xx} = 2 \sum_{\substack{k=-N \\ k \neq 0}}^N \Re \left\{ k \left[ \frac{\mu_1^2}{\omega_1'(\zeta_1)} \zeta_1^{k-1} + \frac{\mu_2^2 C}{\omega_2'(\zeta_2)} \zeta_2^{k-1} \right] A_k \right.$$

$$-\left[\frac{k\mu_2^2 B}{\omega_2'(\zeta_2)}\zeta_2^{-k-1}\right]\bar{A}_k\} \quad (12a)$$

$$\sigma_{yy} = 2 \sum_{\substack{k=-N \\ k \neq 0}}^N \Re \left\{ k \left[ \frac{1}{\omega_1'(\zeta_1)} \zeta_1^{k-1} + \frac{C}{\omega_2'(\zeta_2)} \zeta_2^{k-1} \right] A_k - \left[ \frac{kB}{\omega_2'(\zeta_2)} \zeta_2^{-k-1} \right] \bar{A}_k \right\} \quad (12b)$$

$$\sigma_{xy} = -2 \sum_{\substack{k=-N \\ k \neq 0}}^N \Re \left\{ k \left[ \frac{\mu_1}{\omega_1'(\zeta_1)} \zeta_1^{k-1} + \frac{\mu_2 C}{\omega_2'(\zeta_2)} \zeta_2^{k-1} \right] A_k - \left[ \frac{k\mu_2 B}{\omega_2'(\zeta_2)} \zeta_2^{-k-1} \right] \bar{A}_k \right\} \quad (12c)$$

where the only unknowns in these expressions for the stresses, equations (12), are the complex coefficients,  $A_k$ , and all other quantities involve geometry (location). It should be noted that the material presented above is standard and available in Savin<sup>32</sup> and Lekhnitskii<sup>33</sup> and is only included here for sake of completeness. The stress function,  $\Phi(\zeta_1)$ , can also be represented by a Taylor series where both the complicated physical plane  $R_z$  and the traction-free boundary  $\Gamma$  are mapped into a half-plane,  $R_\zeta$ , and the real axis of  $\zeta$ -plane, respectively. Alshaya et al.<sup>24</sup> demonstrated that representing the stress function by a Laurent or Taylor series expansion gives identical results. The thermoelastic data  $S^* = K(\sigma_{xx} + \sigma_{yy})$ , equation (1), can be expressed as

$$S^* = 2K \sum_{\substack{k=-N \\ k \neq 0}}^N \Re \left\{ \left[ \frac{k(\mu_1^2 + 1)}{\omega_1'(\zeta_1)} \zeta_1^{k-1} + \frac{k(\mu_2^2 + 1)C}{\omega_2'(\zeta_2)} \zeta_2^{k-1} \right] A_k - \left[ \frac{k(\mu_2^2 + 1)B}{\omega_2'(\zeta_2)} \zeta_2^{-k-1} \right] \bar{A}_k \right\} \quad (13)$$

where now the complex coefficients,  $A_k$ , can be determined from the TSA measured-thermal signals.

In a matrix notation, the stresses of equations (12) and the thermoelastic data  $S^*$  of equation (13) each forms a system of simultaneous linear equations throughout a region  $R_z$

$$\sigma = \Sigma \mathbf{c} \text{ and } S^* = \mathbf{A} \mathbf{c} \quad (14)$$

where  $\sigma$  contains the corresponding values of  $\sigma_{xx}$ ,  $\sigma_{yy}$ , and  $\sigma_{xy}$  from equations (12) such that  $\sigma = \{\sigma_{xx}, \sigma_{yy}, \sigma_{xy}\}^T$ ,  $S^*$  contains the corresponding values of  $S^*$  from equation (13),  $\mathbf{c}$  contains the  $4N$  real coefficients  $\mathbf{c} = \{a_{-N}, b_{-N}, \dots, a_{-1}, b_{-1}, a_1, b_1, \dots, a_N, b_N\}^T$ , and the matrices  $\Sigma$  and  $\mathbf{A}$  are real and rectangular coefficient matrices whose sizes depend on the number of retained terms  $N$  of the Laurent power

series expansion and are defined in the following equation

$$\Sigma(i, j) = (-1)^{i-1} 2k \Re \times \left[ \mu_1^{i-1} \frac{\zeta_1^{k-1}}{\omega_1'(\zeta_1)} + \mu_2^{i-1} \frac{C \zeta_2^{k-1} - B \zeta_2^{-k-1}}{\omega_2'(\zeta_2)} \right] \quad (15a)$$

$$\Sigma(i, j+1) = (-1)^i 2k \Im \times \left[ \mu_1^{i-1} \frac{\zeta_1^{k-1}}{\omega_1'(\zeta_1)} + \mu_2^{i-1} \frac{C \zeta_2^{k-1} + B \zeta_2^{-k-1}}{\omega_2'(\zeta_2)} \right] \quad (15b)$$

if  $k < 0, j = 2(k + N) + 1, k \neq 0$ , and if  $k > 0, j = 2(k + N) - 1$  and  $i = 1(\Sigma_{yy}), 2(\Sigma_{xy})$  and  $3(\Sigma_{xx})$

$$A(1, j) = 2kK \Re \left[ \frac{\mu_1^2 + 1}{\omega_1'(\zeta_1)} \zeta_1^{k-1} + (\mu_1^2 + 1) \frac{C \zeta_2^{k-1} - B \zeta_2^{-k-1}}{\omega_2'(\zeta_2)} \right] \quad (16a)$$

$$A(1, j+1) = -2kK \Im \left[ \frac{\mu_1^2 + 1}{\omega_1'(\zeta_1)} \zeta_1^{k-1} + (\mu_1^2 + 1) \frac{C \zeta_2^{k-1} + B \zeta_2^{-k-1}}{\omega_2'(\zeta_2)} \right] \quad (16b)$$

Knowing  $S^*$  at various locations with other known boundary and symmetrical conditions allows the best values of unknown coefficients  $\mathbf{c}$  in a least-squares sense to be determined.

**Further comments.** The induced stresses of equations (12) satisfy equilibrium and compatibility by means of conformal mapping and also satisfies traction-free edge conditions by means of analytic continuation techniques. Therefore, the unknown complex coefficients,  $A_k$ , can be determined by satisfying the other boundary and loading conditions around the entire shape. The variables  $\zeta_j = \xi + \mu_j \eta$  are related to the physical locations  $z = x + iy$  through the inverse mapping function  $z_j = \omega_j(\zeta_j)$  of equations (6) through (7).

Conceptually, the loading and displacement boundary conditions around the entire plate can be imposed to evaluate the complex coefficients, and hence determining the individual stresses throughout the full plate, without involving any measured data.<sup>17</sup> Such strict boundary collocation approach might well require hundreds of coefficients to be retained. In addition, the external boundary conditions of engineering situations are often insufficiently well known to apply pure boundary collocation (or theoretical) methods such as the case of approximating the boundary conditions along the bottom edge of the plate, CD, in Figure 1(a) and (b) as a zero-prescribed displacement condition. However, unlike the classical



boundary-value approach, the unknown complex coefficients are determined herein using the measured thermoelastic data from within region  $R_z$  and the individual stresses were evaluated without the knowledge of the far-field geometry and boundary conditions.

### Determination of unknown complex coefficients from thermoelastic data

The interior thermoelastic data,  $S^*$ , at  $m$  different locations, Figures 2 and 3, are chosen to be inside the region  $R^*$ , a subregion of  $R_z$ , with other  $q$  known symmetrical conditions (in terms of  $\sigma_{xy}$ ) at discrete points along the line  $y=0$ . These measured data are employed to form a system of simultaneous linear equations

$$\mathbf{M}_{(m+q) \times 4N} \mathbf{c}_{4N \times 1} = \mathbf{d}_{(m+q) \times 1} \quad (17)$$

where matrix  $\mathbf{M} = [\mathbf{A} \quad \mathbf{\Sigma}]^T$  consists of analytical expression of  $S^*$ , equation (13), and shear stress, equation (12f), and vector  $\mathbf{d} = [\mathbf{S}^* \quad \mathbf{0}]^T$  has the  $m$  thermoelastic signal  $S^*$  values of Figures 2 and 3 and  $q$  discrete points with zero shear stress conditions such that  $m + q \gg 4N$ . The best values of the complex coefficients,  $A_k$ , in a least-squares numerical sense, can then be determined

$$\mathbf{c}_{4N \times 1} = \left( \mathbf{M}_{4N \times (m+q)}^T \mathbf{M}_{(m+q) \times 4N} \right)^{-1} \mathbf{M}_{4N \times (m+q)}^T \mathbf{d}_{(m+q) \times 1} \quad (18)$$

When  $N=1$  ( $k=-1, 1$ ), four coefficients ( $a_{-1}, b_{-1}, a_1, b_1$ ) can be evaluated in a least-squares sense of equation (18), and eight coefficients ( $a_{-2}, b_{-2}, a_{-1}, b_{-1}, a_1, b_1, a_2, b_2$ ) can be evaluated when  $N=2$  ( $k=-2, -1, 1, 2$ ), and so on. Once  $\mathbf{c}$  are known, the individual stresses then are known throughout the region  $R_z$ , including on the traction-free edge  $\Gamma$ , from equations (12).

It is necessary to select the suitable number of retained coefficients,  $N$ , in the stress function. Retaining too few terms will produce inaccurate results while retaining too many will destabilize the matrix  $\mathbf{M}$  of equation (17) due to computer round-off errors. Therefore, the number of retained terms,  $N$ , in the stress function was assessed by monitoring the condition number of the respective matrix  $\mathbf{M}$ , i.e.,  $\kappa(\mathbf{M})$ , and minimizing the root means square (RMS) value of the difference between the experimental thermoelastic data and those predicted by the present hybrid method. Once the complex coefficients,  $\mathbf{c}'$ , were evaluated for a certain value of  $N$  from equation (18), the reconstructed vector of  $\mathbf{d}$  can be evaluated by  $\mathbf{d}' = \mathbf{M}\mathbf{c}'$ . Therefore, the discrepancy between the vector  $\mathbf{d}$  consisting of the measured TSA data (and  $q$  zeros of the known symmetrical conditions) and

the reconstructed vector  $\mathbf{d}'$  is computed by

$$(\mathbf{d} - \mathbf{d}')_{\text{rms}} = \sqrt{\frac{\sum_{i=1}^{m+q} (d_i - d'_i)^2}{m + q}} \quad (19)$$

where  $m$  is the number of measured thermoelastic data and  $q$  is the number of discretely additional imposed conditions. Using the smallest number of coefficients that gives sufficient accuracy will stabilize the matrix  $\mathbf{M}$ , i.e., minimizing  $\kappa(\mathbf{M})$ , and reduce the computation time.

### Evaluating the complex coefficients

To substantiate the robustness and numerical stability of the hybrid method, a numerical experiment was first conducted by employing stress tensor from FE-simulated stresses using FEM-results.<sup>15</sup> The measured TSA data, 300 for the case of the plate in Figure 1(a) and 849 for the case of the plate in Figure 1(b), are selected to be more than the number of unknown complex coefficients,  $A_k$ , in order to reduce the incorporated noise on the measured data. The overdetermined system was solved in MATLAB (Mathworks, Inc., 2018) using the backslash “\” operator.

For the plate subjected to a central-concentrated load of Figure 1(a), the present method requires 12 complex coefficients (24 real coefficients) when using  $m=300$  thermoelastic signals of Figure 2 and  $q=102$  symmetrical conditions, i.e.,  $\sigma_{xy}=0$ , along the line  $y=0$ . The selection was based on the RMS values of equation (19) and the condition number of matrix  $\mathbf{M}$  as shown in Figure 5.

Similarly, for the plate subjected to an offset load of Figure 1(b), the present method also requires 12 complex coefficients (24 real coefficients) when using  $m=849$  thermoelastic signals of Figure 3 with no other discretely imposed conditions,  $q=0$ . The selection was also based on the RMS values of equation (19) and the condition number of matrix  $\mathbf{M}$  as shown in Figure 6. The appropriateness of utilizing 12 complex coefficients for centrally and offset loaded plates was also substantiated by comparing the reconstructed and measured experimental data using the hybrid methods with the TSA data.<sup>15</sup>

### Airy stress function in real variables

For isotropic, elasto-static response in the absence of the body forces, stress equilibrium and strain compatibility give the biharmonic equation  $\nabla^4 \Phi = 0$ , where  $\Phi$  here is the Airy stress function and  $\nabla^2$  is the Laplacian operator such that  $\nabla^4 = \nabla^2(\nabla^2)$ . The general solution of the biharmonic equation in polar coordinates obtained by Mitchell (1899) is given in Soutas-Little.<sup>37</sup> The general solution contains numerous coefficients (theoretically infinite), called Airy

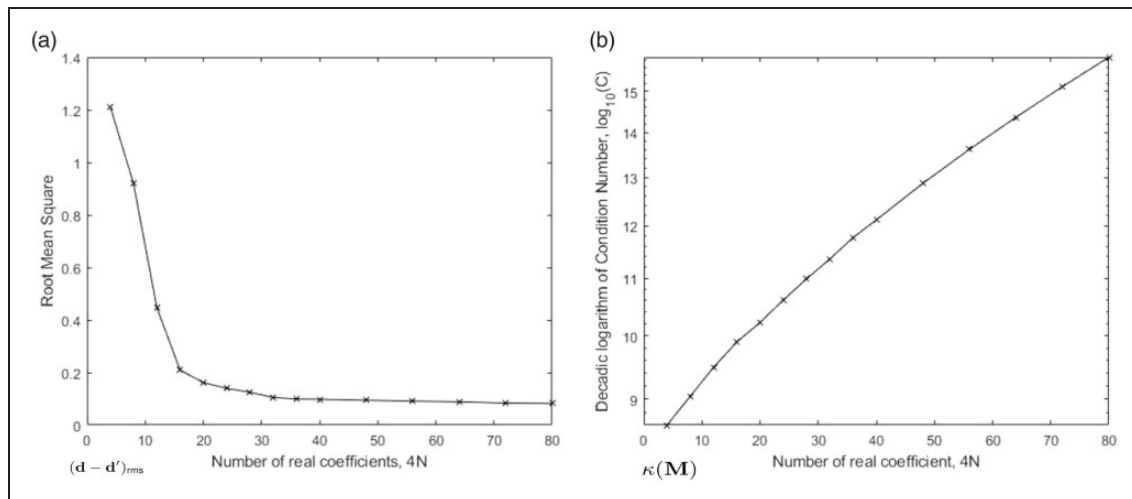


**Figure 5.** The (a) RMS from equation (19) and (b) the condition number of matrix  $\mathbf{M}$  as function of number of retained real coefficients,  $4N$  in the stress function for the plate of Figure 1(a).

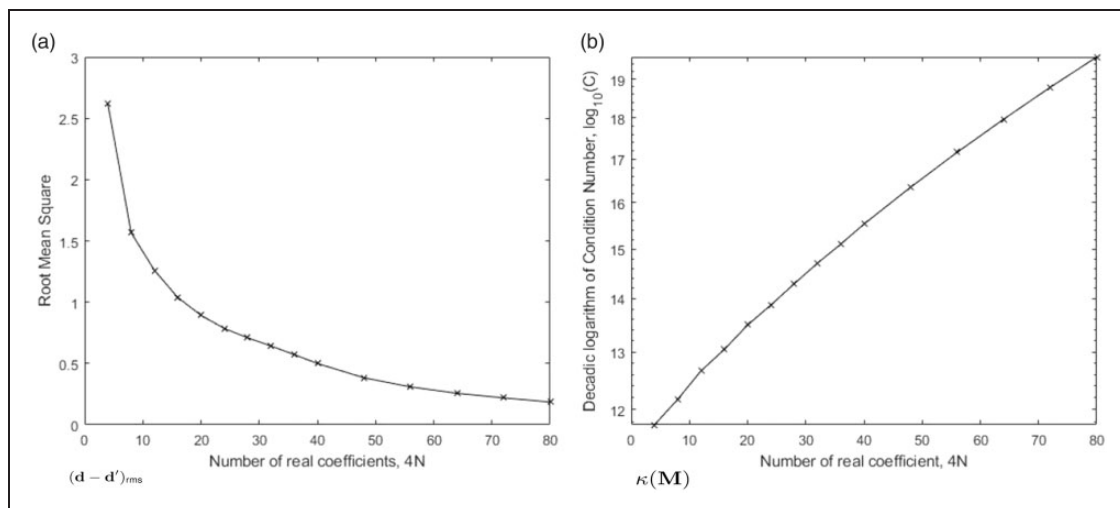


**Figure 6.** The (a) RMS from equation (19) and (b) the condition number of matrix  $\mathbf{M}$  as function of number of retained real coefficients,  $4N$  in the stress function for the plate of Figure 1(b).

coefficients, and which can be reduced by utilizing symmetry and/or satisfying the traction-free condition around the circular hole. Khaja and Rowlands<sup>9</sup> used the general solution of Airy stress function to solve for the hybrid stresses from the thermoelastic data. This approach is referred to herein as *Simple Airy stress method*. In contrast with previous reference and the current approach, literatures<sup>7,8</sup> accounted for the effect of the applied concentrated load  $P$  in the plates of Figure 1(a) and (b) by superposing the general solution of the Airy stress function with the Flament solution (1892) of a concentrated load on semi-infinite plane. This approach is referred to herein as the *Superposition method*. For the sake of comparison only, the hybrid results based on the simple Airy stress method and the superposition method were reproduced here.<sup>15</sup> Based on the same concept of minimizing the root mean square values between the measured TSA and the reconstructed

vector, the hybrid simple Airy stress method and hybrid superposition method require 15 and 24 coefficients for the centrally loaded plate of Figure 1(a) and 25 and 31 coefficients for the offset-loaded plate of Figure 1(b), respectively, as listed in Table 2.

## Results

For convenience, the stresses were normalized with respect to  $\sigma_0$  calculated based on the subjected edge load  $P$  over the gross cross-sectional area, i.e.,  $\sigma_0 = P/(Wt) = 889.6 \text{ N}/(88.9 \text{ mm} \times 88.9 \text{ mm}) = 1.05 \text{ MPa}$ . All the obtained results of the hybrid stresses based on the CVM, Airy stress function (Mitchell solution), superposition of Flament and Mitchell solutions were determined by evaluating the unknown coefficients from the same TSA data shown in Figures 2 and 3 for the centrally loaded plate in Figure 1(a) and offset-loaded plate in Figure 1(b), respectively.

**Table 2.** The number of retained real coefficients,  $k$ , and the stress concentration factor (SCF) for the current analysis, simple airy stress method, and superposition method of the centrally and offset-loaded plates in Figure 1(a) and (b).

	Centrally loaded plate			Offset-loaded plate		
	Current analysis	Simple airy stress method	Superposition method	Current analysis	Simple airy stress method	Superposition method
$k$	24	15	24	24	25	31
SCF	15.8	13.6	16.6	13.7	12.8	14.0

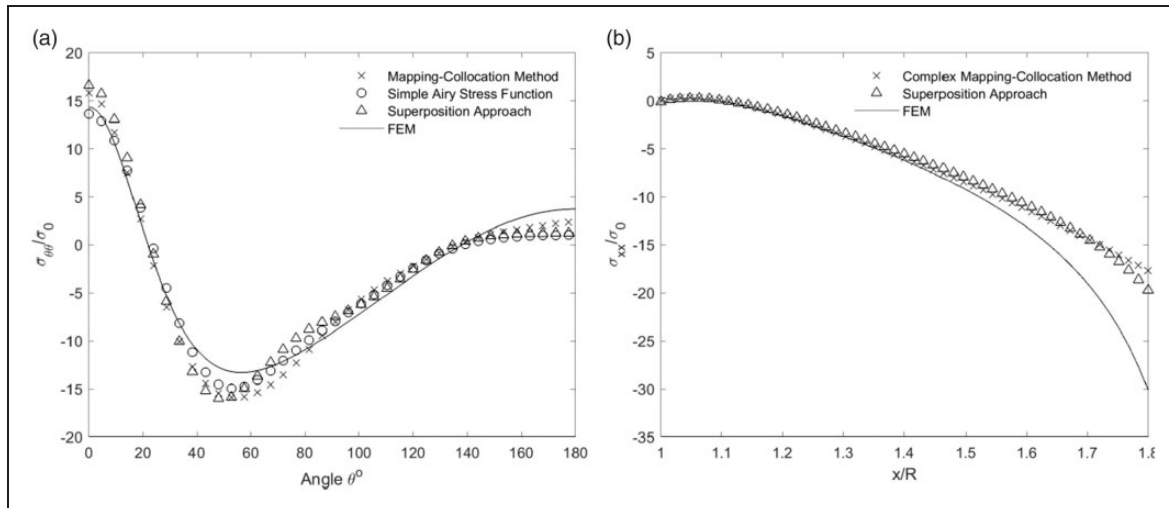


**Figure 7.** Variation of (a)  $\sigma_{\theta\theta}/\sigma_0$  along the boundary of the hole and (b)  $\sigma_{xx}/\sigma_0$  along the line  $y=0$  of Figure 1(a) from FEM, complex variable method (24 real coefficients), simple Airy stress method (15 coefficients), and superposition method (24 coefficients).

### Centrally loaded plate

For the centrally loaded plate in Figure 1(a), the hybrid tangential stress,  $\sigma_{\theta\theta}$ , normalized by the far-field stress,  $\sigma_0$ , are plotted on the boundary of the near-surface circular hole as illustrated in Figure 7. These TSA-based results agree with the FEM predictions. The FEM-prediction and hybrid-TSA using simple Airy stress method (15 coefficients), superposition method (24 coefficients), and CVM (24 real coefficients,  $N=6$ ) determine the stress concentrations at the near-surface circular hole with the values of 14.4, 13.6, 16.6, and 15.8, respectively, as listed in Table 2. The variation of hybrid- $\sigma_{xx}/\sigma_0$  along the line  $y=0$  of Figure 1(a) from FEM, superposition method, and CVM are demonstrated in Figure 7. It shows that the hybrid-TSA results based on superposition method and the CVM predict the stresses beneath the concentrated load very well. In addition to the fact that  $r/R \geq 1.5$  is approaching the location of the applied load and the superposition method explicitly considers the contribution of the concentrated load,  $P$ , the present TSA-determined  $\sigma_{xx}$  along the line  $y=0$  and away from the hole provides reliable stresses comparing to FEM and superposition method. Moreover, the FEM modeled the load, which was physically applied through a piece of round drill

rod, as a top concentrated load acted on a single node.<sup>15</sup>

The contour plots of the normalized polar components of stress from the hybrid CVM (the left part of each figure) and the FEM-predictions (the right part for each figure) in the region adjacent to the near-surface hole are plotted in Figure 8. These figures show an excellent agreement between the FEM-predictions and the hybrid technique using thermoelastic data ( $m=300$  data points and  $q=102$  discretely imposed symmetrical conditions, i.e.,  $\sigma_{xy}=0$ , along the line  $y=0$  in Figure 1(a)).

### Offset-loaded plate

Normalized hybrid tangential stress,  $\sigma_{\theta\theta}/\sigma_0$ , along the boundary of the hole for the offset-loaded plate of Figure 1(b) are depicted in Figure 9(a). The figure shows an excellent agreement between the FEM-predictions and the hybrid-TSA methods. The FEM-prediction and hybrid-TSA using simple Airy stress method (25 coefficients), superposition method (31 coefficients), and CVM (24 real coefficients,  $N=6$ ) determine the stress concentrations at the near-surface circular hole with the values of 10.6, 12.8, 14.0, and 13.7, respectively, as listed in Table 2. The variation of normalized tangential stress,  $\sigma_{\theta\theta}/\sigma_0$ , in the range of

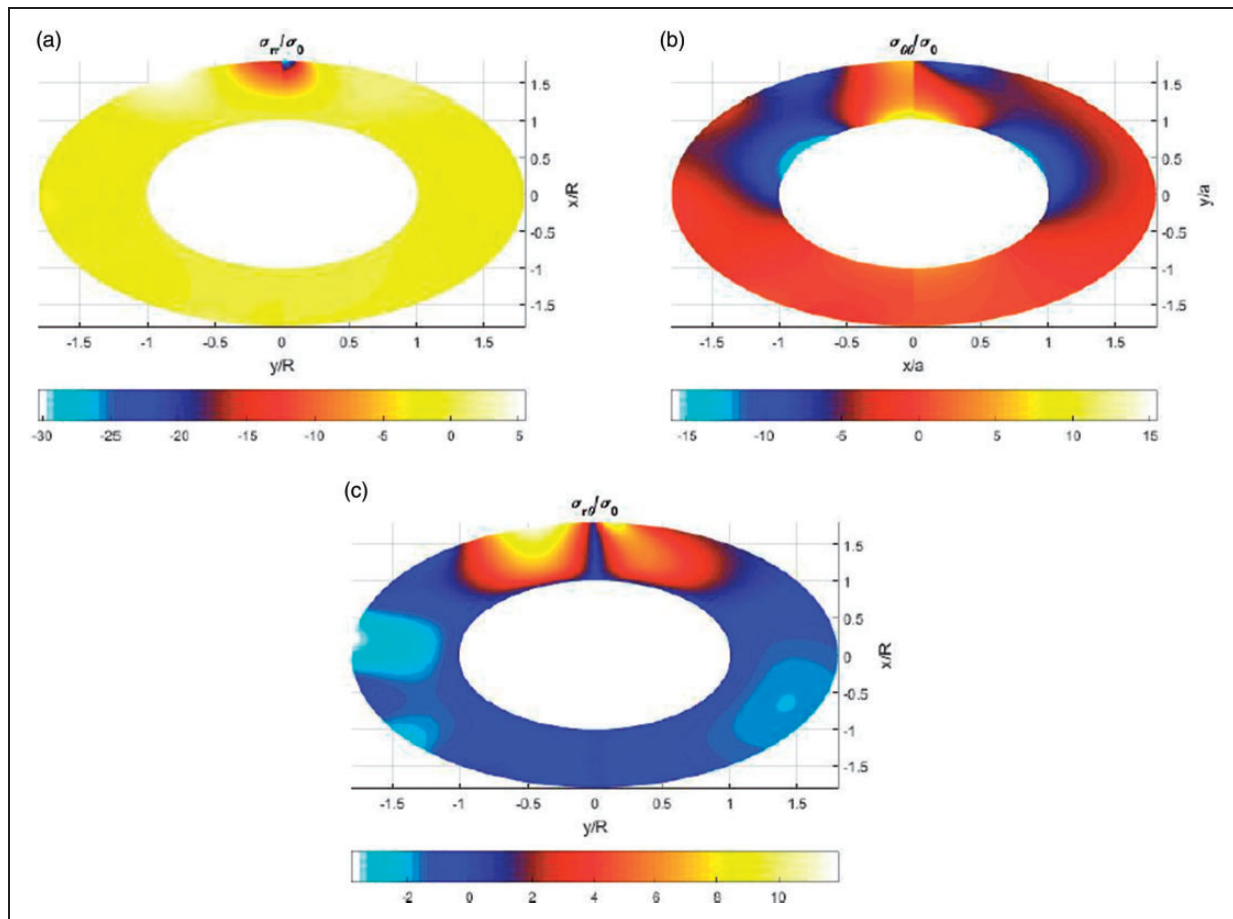


**Figure 8.** Contour plots of (a)  $\sigma_{rr}/\sigma_0$ , (b)  $\sigma_{\theta\theta}/\sigma_0$ , and (c)  $\sigma_{r\theta}/\sigma_0$  throughout the region adjacent to the hole of the plate in Figure 1(a) by the FEM-prediction (right) and the hybrid-TSA based on complex-variable method (left).

$r/R = 1.24$  is shown in Figure 9(b). The only reason of utilizing the location of  $r/R = 1.24$  in Figure 9(b) is to show the continuing reliability of the hybrid-TSA method as moving away from the hole boundary. Even though the model of the FEA was based on assuming the physically applied load as a concentrated load, it was desired to compare these TSA-determined results with FEM-predictions.

The contour plots of the normalized tangential stress,  $\sigma_{\theta\theta}/\sigma_0$ , throughout the region adjacent to the near-surface hole from the hybrid-TSA approaches based on CVM, simple Airy stress method, superposition method, and the FEM-predictions are plotted in Figure 10. These figures show an excellent agreement between the hybrid complex-variable techniques using thermoelastic data ( $m = 849$  data points) and the FEM-predicted values.

The results of the hybrid-TSA approach based on the CVM agree with those from FEM and the hybrid-TSA approaches based on simple Airy stress method and superposition method. The absence of distant geometry and external boundary conditions, including the concentrated load  $P$ , in the stress components of equations (12) indicates that the current approach could handle inverse problem. For example, the magnitude of the applied load  $P$  can be determined by

integrating numerically the vertical stress,  $\sigma_{xx}$ , over the horizontal distance  $-W/2 \leq y \leq W/2$  at some value of  $x$ . This of course requires to utilize the entire TSA data of Figures 2 and 3. Recently, the thermomechanical coefficient of equation (1) and the elastic constants of an orthotropic perforated plate were determined in inverse approach based on the CVM and thermoelastic data.<sup>38</sup>

## Discussion and conclusions

The state of stress on and adjacent to a near-surface hole in finite structures was determined from recorded thermal-stress data. The complex geometry of the plates in Figure 1(a) and (b) was simplified and the equilibrium and compatibility conditions were analytically satisfied by means of conformal mapping and Airy stress function. Utilizing the concept of analytic continuation, the traction-free condition along the boundary of the near-surface hole was also satisfied. Therefore, the presented hybrid-TSA approach is based on strong mechanics foundations. The unknown coefficients of the stress functions were then determined in a least-square sense from the recorded TSA data of Figures 2 and 3. The TSA-hybrid method smooths the actual measured information.



Even though no recorded TSA data were used on and near the edges, the hybrid-TSA approach was able to reliably separate the thermoelastic data into the individual stress components and to accurately evaluate the boundary information.

Unlike earlier approaches<sup>7-9</sup> based on a complicated stress function resulted from an extensive algebra to analytically impose the traction-free condition around the hole and explicitly include the effect of the applied load, excellent results are obtained here using CVM. The present hybrid-TSA approach based on CVM was compared with earlier approaches using the same number and source locations of the measured TSA input values (Figures 2 and 3). For the case of offset-loaded plate of Figure 1(b), the hybrid-TSA approach based on CVM necessitates retaining only 24 coefficients compared to 25 coefficients using simple Airy stress method and 31 coefficient using superposition method. In addition to the fact that the current method provides excellent results comparing with earlier approaches, it involves less algebraic manipulation and in general it can be applied for symmetrical and asymmetrical cases.

The photoelasticity stress analysis requires nonlinear least-squares and displacement-based experimental technique requires differentiating the measured information and the knowledge of the material elastic properties. The numerical-based techniques such as finite-element analyses and boundary-collocation techniques require the full knowledge of the far-field geometry and boundary and loading conditions. The theoretical approach is usually limited to simple, infinite geometries. Unlike the previous techniques, the present TSA-hybrid method requires linear least-squares, is suitable for finite and infinite geometries, does not differentiate the measure data, and does not require the knowledge of the material properties, distant geometry, and boundary and

loading conditions. The numerical computations of the present approach are relatively simple, consume little computer time, and do not require numerically integrating or differentiating procedures. However, the present approach does not guarantee the correct boundary conditions on the rest of the traction-free boundary of the near-surface hole as the traditional boundary-collocation approach. The quality of the evaluated hybrid stresses would deteriorate as the dimension of the interest region becomes large. The size of interest region,  $R_z$ , over which the reliable stress are evaluated can be increased by additionally employing more measured load-induced signals of Figures 2 and 3 in region  $R^*$  and imposing some other boundary conditions. However, the objective herein is to determine reliable stress along, and adjacent to, the near-surface hole boundary, where the interested region is, rather than to evaluate the full-field stresses throughout the entire structure.

Figures 7–10 show a good agreement between the TSA-determined stresses with finite-element results. It should be noted that the discrepancies between FEM and TSA-determined results in Figures 7–10 are due to the fact that the assumed model of FEM might not well represent exactly the actual boundary conditions. In addition to the assumption of the actual physical load applied through a piece of round drill rod as a point concentrated force, the bottom edge of the plate, CD, in Figure 1(a) and (b) was based on the assumption of zero displacements in the vertical direction. The nonuniformity of the stress along the bottom edge of the plate as shown in Figures 2 and 3 does not support this assumption. Therefore, the hybrid results in Lin et al.<sup>7,8</sup> were validated using strain gages measurements. The present results based on CVM agreed very well with results obtained using Mitchell solutions. The boundary-collocation concepts are based on evaluating the unknown

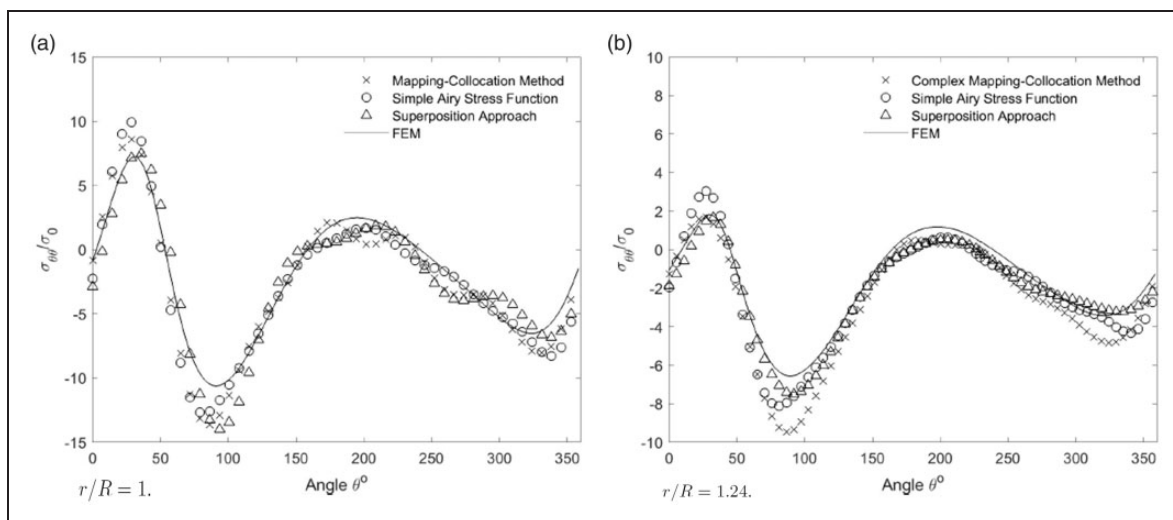


**Figure 9.** Variation of (a)  $\sigma_{\theta\theta}/\sigma_0$  along the boundary of the hole and (b) along  $r/R = 1.24$  of Figure 1(b) from FEM, complex variable method (24 real coefficients), simple Airy stress method (25 coefficients), and superposition method (31 coefficients).

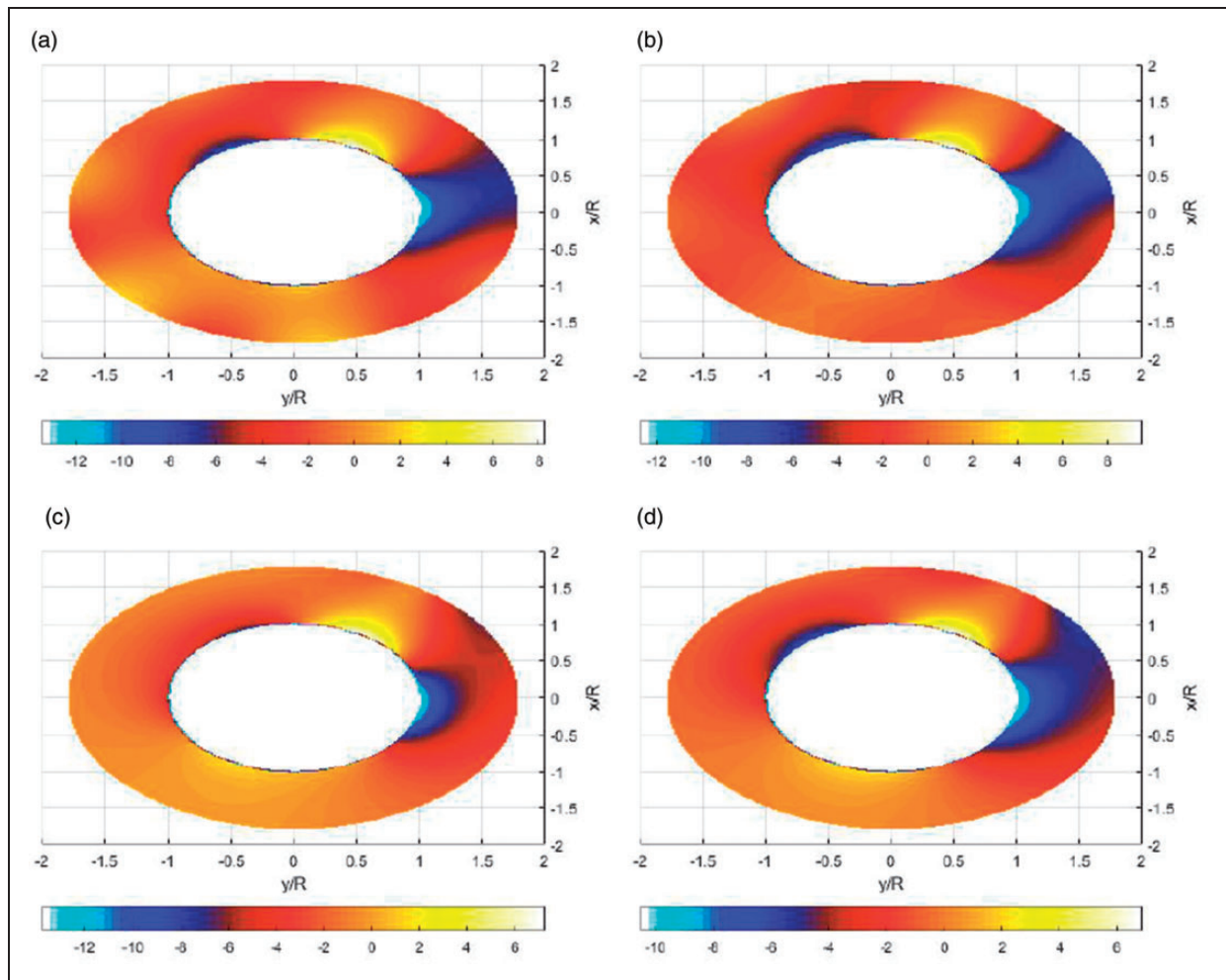


**Figure 10.** Contour plots of  $\sigma_{\theta\theta}/\sigma_0$  throughout the region adjacent to the hole of the plate in Figure 1(b) from (a) hybrid-TSA based on complex-variable method, (b) simple Airy stress method, (c) superposition method, and (d) FEM-predictions.

coefficients in the stress function from the known external loading and boundary conditions, and hence determining the stresses. The insufficient knowledge of the boundary conditions and external loading acting on the structural engineering member can, therefore, preclude using boundary-collocation method. Therefore, this approach is applicable irrespective of the form or magnitude of the loading and the type of boundary condition.

A motivation for developing the present method is to stress-analyze structure with complex geometry without the need of imposing the external boundary and loading conditions. Even though the present analysis can stress-analyze loaded structure which cannot be analyzed numerically, the present geometry (finite plate with near-surface hole), the boundary condition along the bottom edge of the plate (zero-vertical displacement), and the external physical loading (concentrated load) were quite known so FEM modeling was straight forward. However, engineering cases often involve unknown boundary and loading conditions rendering it difficult to reliably model the situation numerically, thereby necessitating such

experimental capabilities such as presented here. Acknowledging the reality that many structures are made of composite materials, the present paper provides the background equations to stress-analyze such plates fabricated from orthotropic composites.

The analysis herein involves a circular hole (whose mapping function is readily available) in a square plate subjected to concentrated edge loads and thermal input data from TSA, but the method can also be applied to various-shaped and more complicated discontinuities and different input experimental data, e.g., strain gages, moiré, DIC, or photoelasticity. Any realistically shaped cutout can be mapped into the exterior region of unit circle by employing Schwarz–Christoffel transformation. The reason of using a circular hole in finite plate subjected to central- and offset concentrated load is to demonstrate the ability of the hybrid method based on CVM to analyze unsymmetrical response while retaining all terms in Laurent series expansion. Future applications of the hybrid CVM could include stress-analysis of anisotropic material and/or finite plate with highly complicated irregular shaped cutouts.

In summary, the present hybrid-technique based on CVM for separating the thermal-induced stresses into the three individual stresses in a finite square plate having a near-surface hole and made of isotropic materials (can also be applied to orthotropic) is extremely effective. The simplicity of the method and ease of implementation by virtually any commercial computation program render it convenient for experimental analysis. This paper emphasizes the concept of demonstrating the hybrid technique based on CVM to determine the state of stress on and adjacent to a near-surface hole in finite structures.

### Acknowledgements

The authors thank Springer Science and Business Media and Elsevier for kindly giving permission to reprint Figures 2 and 3, respectively.

### Declaration of Conflicting Interests

The author(s) declared no potential conflicts of interest with respect to the research, authorship, and/or publication of this article.

### Funding

The author(s) received no financial support for the research, authorship, and/or publication of this article.

### ORCID iD

Abdullah Alshaya  <https://orcid.org/0000-0002-9105-5300>

### References

1. Dulieu-Barton JM and Stanley P. Development and applications of thermoelastic stress analysis. *J Strain Anal Eng Des* 1998; 33: 93–104.
2. Rauch BJ and Rowlands RE. Thermoelastic stress analysis. In: William N Sharpe (ed) *Handbook of experimental mechanics*. 2nd ed. New York: VCH Publishers, 1993, pp.743–763.
3. Greene RJ, Patterson EA and Rowlands RE. Thermoelastic stress analysis. In: Sharpe J and William N (eds) *Springer handbook of experimental solid mechanics*. New York: Springer US, 2008, pp.743–768.
4. Stanley P. Appraisal of a new infrared-based stress analysis technique. *Opt Eng* 1987; 26: 75–80.
5. Stanley P. Applications and potential of thermoelastic stress analysis. *Achiev Mech Mater Eng* 1997; 64: 359–370.
6. Wang WC, Chen YM, Lin MS, et al. Investigation of the stress field of a near-surface circular hole. *Exp Mech* 2005; 45: 244–249.
7. Lin SJ, Quinn S, Matthys D, et al. Thermoelastic determination of individual stresses in vicinity of a near-edge hole beneath a concentrated load. *Exp Mech* 2011; 51: 797–814.
8. Lin S, Matthys D, Quinn S, et al. Stresses at and in the neighborhood of a near-edge hole in a plate subjected to an offset load from measured temperatures. *Eur J Mech A/Solids* 2013; 39: 209–217.
9. Khaja AA and Rowlands RE. Experimentally determined stresses at geometric discontinuities using simple stress functions. *J Eng Mech* 2015; 141: 04015042.
10. Lin SJ, Matthys DR and Rowlands RE. Separating stresses thermoelastically in a central circularly perforated plate using an airy stress function. *Strain* 2009; 45: 516–526.
11. Khaja AA and Rowlands RE. Experimentally determined stresses associated with elliptical holes using polar coordinates. *Strain* 2013; 49: 116–124.
12. Samad W and Rowlands R. Full-field thermoelastic stress analysis of a finite structure containing an irregularly-shaped hole. *Exp Mech* 2014; 54: 457–469.
13. Samad W and Rowlands R. Individual stress determination in irregularly perforated unsymmetrically-loaded structures from temperature data. *Aerospace Sci Technol* 2017; 63: 91–99.
14. Philip SK and Rowlands RE. Thermoelastic stress analysis of a finite structure containing an asymmetrical-oriented, arbitrarily-shaped hole. *J Mech Eng Autom* 2017; 7: 145–159.
15. Alshaya AA. *Experimental, analytical and numerical analyses of orthotropic materials and biomechanics application*. PhD Thesis, University of Wisconsin-Madison, Madison, WI, 2017.
16. Kalaycioglu B, Alshaya A and Rowlands R. Experimental stress analysis of an arbitrary geometry containing irregularly shaped hole. *Strain* 2019; 55: e12306.
17. Singh G and Bhandakkar TK. Simplified approach to solution of mixed boundary value problems on homogeneous circular domain in elasticity. *J Appl Mech* 2018; 86: 021007.
18. Pan Z, Cheng Y and Liu J. Stress analysis of a finite plate with a rectangular hole subjected to uniaxial tension using modified stress functions. *Int J Mech Sci* 2013; 75: 265–277.
19. Jafari M and Ardalani E. Stress concentration in finite metallic plates with regular holes. *Int J Mech Sci* 2016; 106: 220–230.
20. Lin ST and Rowlands RE. Thermoelastic stress analysis of orthotropic composites. *Exp Mech* 1995; 35: 257–265.
21. Rhee J and Rowlands R. Thermoelastic-numerical hybrid analysis of holes and cracks in composites. *Exp Mech* 1999; 39: 349–355.
22. Ju SH and Rowlands R. Mixed-mode thermoelastic fracture analysis of orthotropic composites. *Int J Fract* 2003; 120: 601–621.
23. Ju SH and Rowlands RE. Thermoelastic determination of KI and KII in an orthotropic graphite-epoxy composite. *J Compos Mater* 2003; 37: 2011–2025.
24. Alshaya A, Shuai X and Rowlands R. Thermoelastic stress analysis of a finite orthotropic composite containing an elliptical hole. *Exp Mech* 2016; 56: 1373–1384.
25. Hawong JS, Lin CH, Lin ST, et al. A hybrid method to determine individual stresses in orthotropic composites using only measured isochromatic data. *J Compos Mater* 1995; 29: 2366–2387.
26. Baek T and Rowlands R. Hybrid stress analysis of perforated composites using strain gages. *Exp Mech* 2001; 41: 195–203.
27. Baek TH and Rowlands RE. Experimental determination of stress concentrations in orthotropic composites. *J Strain Anal Eng Des* 1999; 34: 69–81.
28. Alshaya A and Rowlands R. Experimental stress analysis of a notched finite composite tensile plate. *Compos Sci Technol* 2017; 144: 89–99.

29. Stanley P and Chan WK. Quantitative stress analysis by means of the thermoelastic effect. *J Strain Anal Eng Des* 1985; 20: 129–137.
30. Dulieu-Smith J and Stanley P. On the interpretation and significance of the Grüneisen parameter in thermoelastic stress analysis. *J Mater Process Technol* 1998; 78: 75–83.
31. Lin SJK. *Two-and three-dimensional hybrid photomechanical-numerical stress analysis*. PhD Thesis, University of Wisconsin-Madison, Madison, WI, 2007.
32. Savin GN. *Stress concentration around holes*. Pergamon: Pergamon Press, 1961.
33. Lekhnitskii SG. *Theory of elasticity of an anisotropic elastic body*. 1st ed. San Francisco: Holden-Day, 1963.
34. Gerhardt TD. A hybrid/finite element approach for stress analysis of notched anisotropic materials. *J Appl Mech* 1984; 51: 804–810.
35. Bowie O and Freese C. Central crack in plane orthotropic rectangular sheet. *Int J Fract Mech* 1972; 8: 49–57.
36. Huang YM. *Determination of individual stresses from thermoelastically measured trace of stress tensor*. PhD Thesis, University of Wisconsin-Madison, Madison, WI, 1989.
37. Soutas-Little RW. *Elasticity*. Mineola: Dover Publications, 1999.
38. Alshaya AA and Considine JM. Determination of constitutive parameters in inverse problem using thermoelastic data. In: Baldi A, Quinn S, Balandraud X, Dulieu-Barton J and Bossuyt S (eds) *residual stress, thermomechanics & infrared imaging, hybrid techniques and inverse problems, vol. 7*. New York: Springer International Publishing, pp.25–34.

## Appendix

### Notation

$\mathbf{A}$	coefficient matrix for isopachic stress
$A_k$	complex coefficients $A_k = a_k + ib_k$
$\bar{A}_k$	complex conjugate of $A_k$
$B, C$	constants depend on material properties
$\mathbf{c}$	vector of the 4 $N$ unknown real coefficients
CVM	complex-variable method
$\mathbf{d}$	vector of $m$ measured thermoelastic data in addition to $q$ zeros from symmetrical conditions
$D$	vertical distance between the hole center to the applied load
$E$	modulus of Elasticity or the horizontal distance between the hole center to the applied load
$E_1, E_2$	elastic moduli in material directions
$G_{12}, G$	shear modulus
$\Im$	imaginary part of the complex number
$k$	number of retained coefficients

$K$	thermoelastic calibration coefficient
$L$	height of the plate
$m$	number of measured input thermoelastic (load-induced) data
$\mathbf{M}$	matrix $\mathbf{M} = [\mathbf{A} \quad \mathbf{\Sigma}]^T$
$N$	terminating integer of the summation series
$P$	applied concentrated load
$q$	number of imposed symmetrical conditions
$r, \theta$	polar coordinates
$R$	radius of hole
$R^*$	region of selected data
$\Re$	real part of the complex number
$R_z$	region in the physical plane ( $x, y$ )
$R_\zeta$	mapped region of $R_z$ in $\zeta$ -plane ( $\xi, \eta$ )
RMS	root mean square
$S^*$	thermoelastic load-induced temperature signals
$\mathbf{S}^*$	vector of $m$ measured thermoelastic data
SCF	stress concentration factor
$t$	thickness of the plate
$W$	width of the plate
$x, y$	Cartesian (rectangular) coordinates in the physical plane
$z_1, z_2$	complex variables; $z_j = x + \mu_j y$ for $j = 1, 2$
$\alpha$ and $\gamma$	distinct real parts of complex parameters $\mu_k$
$\beta$ and $\delta$	distinct imaginary parts of complex parameters $\mu_k$
$\Gamma$	traction-free boundary in the physical plane $R_z$
$\Gamma_\zeta$	mapped traction-free boundary, $\Gamma$ , in the $\zeta$ -plane $R_\zeta$
$\kappa(\mathbf{M})$	condition number of matrix $\mathbf{M}$
$\zeta, \xi, \eta$	coordinates in mapped plane
$\mu_k$	roots of characteristic equation associated with compatibility equation
$\nu_{12}, \nu$	Poisson's ratio
$\sigma_0$	far-field applied normal stress, $\sigma_0 = P/(Wt)$
$\sigma_p, \sigma_q$	principal stresses
$\sigma_{rr}, \sigma_{\theta\theta}, \sigma_{r\theta}$	stresses in polar coordinates (radial, tangential, and shear stresses)
$\sigma_{xx}, \sigma_{yy}, \sigma_{xy}$	stresses in Cartesian coordinates
$\boldsymbol{\sigma}$	stress vector, $\boldsymbol{\sigma} = \{\sigma_{xx}, \sigma_{yy}, \sigma_{xy}\}^T$
$\mathbf{\Sigma}$	coefficient matrix for stresses
$\sum$	summation
$\Phi(z_1)$	stress function $\Phi(z_1) = dF_1(z_1)/dz_1$
$\Psi(z_1)$	stress function $\Psi(z_1) = dF_2(z_2)/dz_2$
$\omega(\zeta)$	mapping function
$\backslash$	backslash operator (MATLAB)
$\nabla^2$	Laplacian operator